

# Improved Identifiability of Kinetic Parameters in Lithium-Ion Batteries via Nonlinear Frequency Response Analysis

Hoon Seng Chan, Yan Ying Lee, Daniel Witt, Julian Ulrich, André Weber, and Ulrike Krewer\*

Model parameterization is essential, on one side, to offer insights into the internal states of a Li-ion battery, and on the other side, to deliver realistic predictions of the battery performance. Multistep parameterization, including the C-rate test, electrochemical impedance spectroscopy, and for the first time, nonlinear frequency response analysis, has been implemented in this study. Via nonlinear frequency response analysis, an asymmetrical charge transfer process at the positive electrode is identified, whereby the charge transfer coefficient at the positive electrode

is no longer 0.5, as assumed in many simulation works. Further, it is shown that nonlinear frequency response analysis in combination with electrochemical impedance spectroscopy can improve the uniqueness of the kinetic model parameters. Specifically, ambiguous sets of kinetic parameters, that is, rate constant and charge transfer coefficient, are identified via only electrochemical impedance spectroscopy. The ambiguity can be resolved with additional nonlinear frequency response analysis.

## 1. Introduction

Battery modeling is beneficial for predicting the performance of lithium-ion batteries (LiBs) under different operating conditions.<sup>[1,2]</sup> They allow to predict state-of-charge relative to the maximum capacity or state-of-health of the battery, that is, the degradation of the maximum capacity during aging.<sup>[3,4]</sup> Also, battery modeling is shown to be useful in determining the operating limits to avoid significant harm such as lithium plating<sup>[5]</sup> or thermal runaway<sup>[6]</sup> to LiBs. In addition, battery models aid in optimizing the internal structure of batteries, such as electrode thickness, chemistries, or particle size distribution for a specific application.<sup>[7,8]</sup> There are various modeling approaches, which differ in complexity, physical insights, capabilities, and limitations.<sup>[9]</sup> Mechanistic models use first principle approaches to describe the processes within the battery and therefore offer the most comprehensive and insightful modeling of the battery dynamics. Such models are usually complicated and computationally expensive.<sup>[10,11]</sup> Semiempirical approaches such as equivalent circuit models use electrical circuit components to depict the process dynamics within the batteries. This approach is popular as it retains some degree of physical insights. It is typically used in state estimation in battery management systems.<sup>[12,13]</sup> Unlike mechanistic and semiempirical models, data-driven models do

not reveal any physical insights, and they depend heavily on the quantity and quality of the training data.<sup>[14,15]</sup>

The Doyle–Fuller–Newman model, also known as the pseudo-two-dimensional (P2D) model, is the most common and widely implemented battery model at the cell level.<sup>[16]</sup> The governing equations in the P2D model contain transport and charge conservation of lithium ions within the solid and electrolyte phases as well as the charge transfer kinetics at the electrode/electrolyte interface. Legrand et al.<sup>[17]</sup> further added the double-layer capacitance effect into the P2D model, which enables the simulation of electrochemical impedance behavior (EIS) of LiBs. Until now, there have been several adaptations or extensions to the classical P2D model that consider different degradation mechanisms in the LiBs, for example, the formation and growth of solid electrolyte interphase (SEI) film<sup>[18–20]</sup> and lithium plating.<sup>[5,21,22]</sup> In this work, we will implement the SEI-extended P2D model established by Witt et al. which models the additional process kinetics at the SEI/electrolyte interface as well as lithium-ion transport through the SEI layer.<sup>[18,23]</sup>

For a reliable and accurate simulation of the battery behavior with the P2D model, a reliable parameterization is essential. The model parameters are either individually determined under specially designed experiments or batch-wise fitted via multistep parameterization. Examples for the first case are the solid diffusion coefficient, which is determined via the galvanostatic Intermittent titration technique (GITT).<sup>[24–26]</sup> Open circuit voltage (OCV) is similarly measured via GITT and fitted in the form of the Redlich–Kister equation.<sup>[27]</sup> Solid electric conductivity can be determined using the four-point probe method.<sup>[28]</sup> Electrolyte properties such as ionic conductivities are determined in platinum microelectrode setup via EIS.<sup>[29]</sup> Lithium-ion binary diffusion coefficient and transference number are determined in lithium metal symmetrical coin cells using pulse experiments.<sup>[29]</sup> Kinetic parameters such as exchange current densities are extracted from EIS.<sup>[28,30,31]</sup>

For multistep parameterization using electrochemical methods on a full cell, the model parameters are grouped and

H. S. Chan, Y. Y. Lee, D. Witt, J. Ulrich, A. Weber, U. Krewer  
Institute for Applied Materials – Electrochemical Technologies  
Karlsruhe Institute of Technology  
Adenauerring 20b, 76131 Karlsruhe, Germany  
E-mail: ulrike.krewer@kit.edu

 Supporting information for this article is available on the WWW under <https://doi.org/10.1002/batt.202500179>

 © 2025 The Author(s). *Batteries & Supercaps* published by Wiley-VCH GmbH. This is an open access article under the terms of the Creative Commons Attribution License, which permits use, distribution and reproduction in any medium, provided the original work is properly cited.

sequentially fitted using a series of electrochemical characterization methods. In conjunction with this, identifiability studies for the P2D model or a simplified version—the single particle model are conducted. Laue et al. concluded that EIS is a crucial complementary electrochemical characterization method as compared to C-rate tests, as some parameters remain ambiguous when using only the conventional OCV and C-rate parameterizations.<sup>[32]</sup> Bizeray et al. pointed out that EIS at a single state-of-charge (SoC) is not sufficient to parameterize the model due to the flat nature of the thermodynamic OCV behavior.<sup>[33]</sup> Laue et al. recommended a multistep parameterization procedure, which includes OCV, C-rate, and EIS, for the full parameterization of the P2D model. The author used OCV to identify mainly static parameters, such as solid concentration in electrodes; C-rate tests for quasi-static parameters, such as diffusion coefficients, tortuosities, electronic conductivities, and exchange current densities; EIS for the fine tuning of dynamic parameters, like double-layer capacitances, and electronic conductivities as well as exchange current densities.<sup>[18,32]</sup> Witt et al. extended the parameterization strategy proposed by Laue et al. to the SEI-extended P2D model to parameterize SEI-related kinetic parameters via EIS.<sup>[18]</sup>

Yet, the charge transfer coefficient is not assessable via the current parameterization procedure even with advanced dynamic analysis such as EIS. Murbach et al. and Wolff et al. showed in their studies that the charge transfer coefficient is not sensitive to EIS.<sup>[34,35]</sup> Murbach et al. further derived analytical solutions of the voltage response signals with respect to EIS as well as higher harmonics and showed that the charge transfer coefficient cannot be uniquely determined via EIS, but the second harmonics may allow a unique identification.<sup>[34]</sup> Alternatively, EIS with applied bias currents was shown to be able to identify the charge transfer coefficient as implemented in Ecker et al. work.<sup>[28]</sup> Nevertheless, this method is challenging because it infringes the time invariance criterion as SoC drifts during the measurement.<sup>[28,36]</sup> Thus, the charge transfer coefficient is usually assumed to be constant at 0.5 in most of the simulations. Further methods were used to determine the charge transfer coefficients. The most common approach is via Tafel plot fitting at a single SoC, and the charge transfer coefficient can be assessed through the slope of the Tafel plot.<sup>[37]</sup> Hess et al. suggested that the charge transfer coefficient can be obtained through the fitting of Butler–Volmer equations using GITT measurement.<sup>[38]</sup> Also, theoretical approaches like density functional theory were used.<sup>[39]</sup> However, they require a very deep and accurate understanding of reaction and materials.

The charge transfer coefficient has been shown to be identifiable with nonlinear characterization methods known as nonlinear electrochemical impedance spectroscopy (NLEIS) or nonlinear frequency response analysis (NFRA). For example, Agarwal et al. and Devanathan et al. both showed on theoretical basis that the charge transfer coefficient is identifiable via nonlinear responses that arise from the electrode process, as the amplitude of the harmonics depends on the difference of cathodic and anodic charge transfer coefficient coefficients.<sup>[40,41]</sup> Later, Darowicki et al. determined the charge transfer coefficient for the oxygen evolution reaction using NLEIS.<sup>[42]</sup> Similarly, Xu et al. implemented a similar approach by applying NLEIS for the determination of charge

transfer coefficient based on the ferri-ferrocyanide redox system.<sup>[43]</sup> Adler implemented the similar method to extract charge transfer coefficient for the mixed-conducting solid oxide fuel-cell cathode. Recently, this nonlinear method has been applied to LiBs to extract additional nonlinear information on LiBs.<sup>[44,45]</sup> Via the nonlinear characterization techniques, Murbach et al. and Wolff et al. demonstrated that the charge transfer coefficient is uniquely sensitive to the second harmonic, which makes the determination of the charge transfer coefficient feasible.<sup>[35,41]</sup> Kirk et al. demonstrated the determination of the charge transfer coefficient via second harmonic in NLEIS on single particle model.<sup>[46]</sup> Ji et al. developed a nonlinear Randle circuit model and performed parameterization using both EIS and NLEIS, where the charge transfer coefficient is determined for fresh and aged cell.<sup>[47,48]</sup> Ulrich et al. performed a model-assisted analysis of plating behavior and estimated the plating-related charge transfer coefficient.<sup>[49]</sup>

In this work, we perform parameterization on a full P2D battery model with SEI, which considers, besides electrode kinetics, also the kinetics of the interfacial process at the SEI layer as well as the transport through it. To better delineate the process kinetics, we carry out parameterization based on three-electrode measurements, which consist of OCV, C-rate tests, EIS, and NFRA. With NFRA, we target a unique and quantitative identification of the kinetic parameters, specifically the charge transfer coefficients. Firstly, the P2D-SEI model of Li-ion battery will be shortly summarized and the proposed multistep parameterization strategy will be detailed. Next, a parameter study is carried out to reveal the relationship between the kinetic parameters and the electrochemical response. Lastly, uniqueness analysis is conducted to reveal the significance of incorporating NFRA into the multistep parameterization strategy.

## 2. Methodology

### 2.1. Modeling Framework

In this work, we employed the SEI-extended P2D model proposed in our previous work.<sup>[18]</sup> The governing equations are summarized in Supporting Information S1. Contrary to the classical P2D model, the proposed model incorporates additional interfacial processes at the SEI/electrolyte interface as well as transport of lithium-ions across the SEI at the negative electrode. Here, it is suggested that during discharge at the negative electrode, lithium first de-intercalates from its host material and transfers to a vacant surface site at the electrode/SEI interface. Then, the lithium-ion is transported across the SEI, driven by potential (migration) and concentration (diffusion) gradients. At the SEI/electrolyte interface, the lithium-ion undergoes solvation and desorption before entering the electrolyte phase. The rate of all interfacial processes at the negative electrode is expressed in the form of Arrhenius equations with detailed descriptions of the forward and backward reaction rates as well as the respective Gibbs free and activation energies. The Gibbs free energies are computed from the chemical potentials of the involved species in the designated interfacial reactions. This makes the expression

of the kinetic rate of different interfacial processes distinctive to each other. Therefore, a unique assignment of the kinetic parameter to the respective rate expression is possible. Meanwhile, at the positive electrode, only one interfacial process, namely Li-ion (de)-intercalation is considered, and its kinetics are described using the classical Butler–Volmer equation. In addition, contact resistances and double-layer capacitances at the interface between the current collector and both negative and positive electrodes are considered.

## 2.2. Nonlinear Frequency Response Analysis

NFRA is for the first time introduced into the multistep parameterization strategy in this study. Similar to EIS, for NFRA simulation, the P2D model is excited galvanostatically but with a higher periodical current signal.

As the model is inherently nonlinear, the voltage responses contain linear as well as nonlinear harmonic signals,<sup>[50]</sup> which can be depicted in the Fourier series. By applying Fourier transformation on the voltage response, the individual harmonic signals can be separated and identified. In this study, only the amplitudes of the harmonic signals are analyzed, that is, the voltage amplitude of the second harmonic,  $Y_2$ , and of the third harmonic,  $Y_3$ . For more information on the method, please refer to.<sup>[35]</sup>

## 2.3. Multistep Parameterization Strategy

The proposed P2D model will be parameterized using an extended sequential multistep parameterization strategy similarly as in our former studies.<sup>[18,32]</sup> The sequential parameterization implies that the parameterization process at each stage builds only upon the measurements at this step and the parameterization results of the previous stages, and no iterative procedure is performed. For the parameterization step 1, the parameters are determined independently. Firstly, the multistep parameterization strategy begins using a low C-rate discharge (e.g., C/10) to extract information on Li inventory (cell balancing) such as maximum Li concentration in active material  $c_{\max}$  and SEI thickness  $d_{\text{SEI}}$ . Afterwards, a high C-rate discharge experiment (here: 1C, 2C) is used for parameterizing Li transport parameters, for instance, solid diffusion coefficients  $D_s$  and tortuosities  $\tau$ . Next, parameters that are sensitive to EIS are determined. These include rate constants for every interfacial reaction  $k_0$ , contact resistances  $R_{cc}$ , double-layer capacitances  $C_m^{\text{DL}}$ , solid electronic conductivities  $\sigma_s$ , as well as the ionic conductivity of the SEI  $\kappa_{\text{SEI}}$ . Lastly, we further extended the multistep parameterization strategy by taking NFRA into consideration. Here, kinetic parameters are refined; in particular, the charge transfer coefficient  $\alpha$  is identified using its distinctive sensitivity toward the second harmonics, as mentioned in,<sup>[35]</sup> and the kinetic parameters obtained from the previous parameterization step (EIS) are further fine-tuned. The proposed multistep parameterization strategy is illustrated in Figure 1.

The multistep parameterization strategy was performed via nonlinear least-squares optimization in MATLAB. For this purpose,

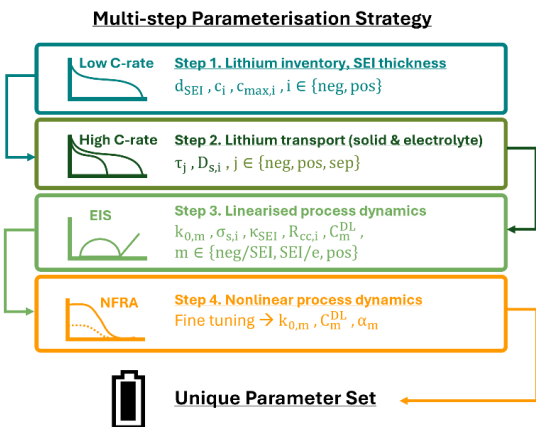


Figure 1. Multistep parameterization strategy with NFRA extension after C-rate and EIS parameterization for the P2D-SEI model.

an objective function that describes the squared relative difference between experiment and simulation for each parameterization step is defined. An optimal parameter set is identified by minimizing the objective function. The definition of the objective functions from step 1 to 3 of the multistep parameterization strategy is similar to our previous work,<sup>[18]</sup> where the half-cell discharge curves and EIS, in the frequency range from 5–1 kHz, are used for parameter identification. For step 4, NFRA is used at full cell level and at positive electrode. Here, the nonlinear frequency response (NFR) spectrum of the negative electrode is neglected as the NFR response arises mainly at low frequency range, where in the EIS, we see a measurement artifact (see also Lee et al.<sup>[51]</sup>). Here, we assume that the NFR is also impacted. Hence, the objective function for the NFRA parameterization is defined as follows

$$F_{\text{NFRA}}(X) = \sum_{j \in \{\text{full, pos}\}} \sum_{k=1}^n \left( \frac{(Y_{2,\text{exp},j}(k) - Y_{2,\text{sim},j}(k))^2}{\max(Y_{2,\text{exp},j})^2} + \frac{(Y_{3,\text{exp},j}(k) - Y_{3,\text{sim},j}(k))^2}{\max(Y_{3,\text{exp},j})^2} \right) \quad (1)$$

$n$  frequencies between 1 and 300 Hz at full cell level as well as at half-cell positive electrode are considered. Based on this approach, the parameters of the positive electrode are identified by using the half-cell positive electrode data while the parameters of the negative electrode are determined by matching the model output to the full-cell response, which does not contain the artifact of the negative electrode measurement, and constraining the model based on prior knowledge of the positive electrode.

## 2.4. Uniqueness Analysis

The uniqueness of the identified kinetic parameters from parameterization without NFRA, that is, omitting the last parameterization step, is evaluated. Similar to our previous work,<sup>[32]</sup> we use an indirect sample-based identifiability test. In this approach, EIS is

simulated via various combinations of parameter sets, which are iteratively sampled in a defined parameter space  $\Omega$ . Here, all other parameters are kept constant to the identified parameter set while kinetic parameters (rate constant  $k_0$  and charge transfer coefficient  $\alpha$ ) are investigated due to the qualitatively similar impact on EIS spectra (see Figure S1 in Supporting Information). In this study,  $k_0$  varies by orders of magnitude, and the corresponding parameter space is logarithmically varied while  $\alpha$  is equidistantly varied.

$$\Omega_\alpha \in [\alpha_{\min}, \alpha_{\max}] \quad (2)$$

$$\Omega_{k_0} \in [\log k_{0,\min}, \log k_{0,\max}] \quad (3)$$

Each parameter range is discretized into 50 points. This results in  $50 \times 50$  combinations of  $\alpha$  and  $k_0$ , for a total of 2500 EIS simulations. In these simulations, EIS spectra are simulated with the same frequency points as the experiment, that is, 10 points per decade above 66 Hz and 5 points per decade below 66 Hz. The residuum between the simulated and the experimental EIS spectra is summed over the probed frequencies  $f_i$  for each parameter sample. A parameter is not unique when more than one set of parameter variations shows a similar residuum  $\Delta Z$ .

$$\Delta Z = \sum_{i=1}^m \sqrt{(Z'_{\text{sim}}(f_i) - Z'_{\text{exp}}(f_i))^2 + (Z''_{\text{sim}}(f_i) - Z''_{\text{exp}}(f_i))^2} \quad (4)$$

All simulations in this work, including multistep parameterization and uniqueness analysis, were performed in MATLAB R2019b.

## 2.5. Experiment

For the parameterization, we used a three-electrode setup (PAT-Cell) from EL-Cell GmbH with electrode materials, that is, lithium nickel manganese cobalt oxides—811 for positive electrode and blends of silicon-graphite (Si content estimated as  $2.8 \pm 0.5$  wt% from postmortem SEM-EDX analysis) for the negative electrode, extracted from a commercial cylindrical cell (LG 18650 HG2), which has a nominal capacity of 3 Ah. The extracted electrode materials were double-sided coated, and therefore, one side of the electrode coating was removed using N-Methyl-2-Pyrrolidone. After that, the electrodes were rinsed several times with dimethyl carbonate and dried under an argon atmosphere before punching into discs with a diameter of 18 mm for the PAT-Cell setup. A 220  $\mu\text{m}$  thick commercial separator (EL-CELL GmbH, ECC1-00-0210 V/X) of polypropylene and polyethylene with a built-in lithium reference ring was used. In addition, we used 103  $\mu\text{L}$  electrolyte, composed of ethylene carbonate and dimethyl carbonate with a ratio of 1:1 v/v and 1 M lithium hexafluorophosphate. The whole cell assembly process was done in an argon-filled glovebox ( $\text{O}_2$  and  $\text{H}_2\text{O} < 0.1$  ppm). After that, the cell was first rested for 12 h in a temperature chamber (MMM Friocell 55) at 25 °C and then subjected to formation and cycled using a battery cycler (BaSyTec CTS Lab). During the formation step, the cells were charged and discharged with C/10 without a

**Table 1.** Measurement parameters and conditions for the C-rate test, EIS and NFRA.

C-rate test		
Voltage range	3.0–4.2 [V]	
Charge current	C/2 (CC-CV, current cutoff at C/20)	
Discharge current	C/2, 1C, 2C (CC)	
Temperature	25 [°C]	
		EIS
		NFRA
Excitation amplitude	500 [ $\mu\text{A}$ ] (C/12)	10 [mA] (1.5 [C])
Frequency range	10 [mHz]–1 [MHz]	100 [mHz]–1 [kHz]
Voltage	4.151 [V] (about SoC 90%)	
Temperature		23 [°C]

constant voltage (CV) phase for two cycles; in the third cycle, a constant current followed by CV until C/20 was applied in the charge direction between 3.0 V and 4.2 V at 25 °C. Next, a C-rate test was performed on the cell via a similar measurement setup. After a rest time, EIS and NFRA measurements were carried out using a Zahner Zennium potentiostat/galvanostat under galvanostatic mode. The measurement parameters for the characterizations are shown in **Table 1**. For EIS and NFRA, the selection of 90% SoC was motivated by the fact at high SoC the charge transfer kinetics for the studied electrode material is more prominent and thus more accessible for electrochemical characterization especially for the nonlinear characterization. As for NFRA, the excitation amplitude of 1.5 C was chosen to ensure a sufficiently strong nonlinear response for reliable NFRA characterization.<sup>[14]</sup> We are aware that high SoC and large perturbation amplitude in NFRA could induce undesired side reactions such as lithium plating, which could then falsify the interpretation outcome. To ensure that no plating had occurred, we monitored the OCV relaxation behavior immediately following the NFRA measurements. No abnormal voltage plateau—often associated with lithium plating/stripping—was observed. Also, an NFRA simulation was performed based on the parameterized model and the potential at the negative electrode does not go below 0 V, which is often associated with the onset of lithium plating (Figure S2 in Supporting Information). Furthermore, the experiments were carried out at room temperature ( $\approx 25$  °C), well above the threshold temperature range where lithium plating typically becomes a concern. Therefore, we concluded that lithium plating is unlikely to happen during the NFR measurement.

## 3. Results and Discussion

In this section, the quality of the result from the multistep parameterization strategy will be analyzed. Next, a parameter study is performed based on the obtained parameter set for the given battery, followed by a uniqueness evaluation to check the sensitivity and uniqueness of the obtained parameter set based on the proposed parameterization strategy.

### 3.1. Parameterization Results via Multistep Parameterization Strategy

Via the proposed parameterization strategy, a parameter set that can reproduce the experimental discharge behavior at different C-rates, EIS and NFRA in full-cell and half-cells is identified for the first time in this work. The comparison between the simulation and the experimental curves is depicted in Figure 2. The obtained parameter set is listed in Table 2.

From Figure 2(a), (d), and (g), one can observe that a good agreement between simulated and experimental discharge behavior at different C-rates is obtained in full-cell as well as half-cells. Meanwhile, a promising match between simulated and experimental EIS and NFR spectra at the full-cell level is shown in Figure 2(b) and (c). Note that at the negative electrode, a measurement artifact, that is, inductive loop, arises in the frequency range below 10 Hz as shown in Figure 2(e). These are known to occur for many measurements with Li reference electrodes, also in our setup.<sup>[51]</sup> Therefore, parameterization of the half-cell level frequency response, especially at the negative electrode is not reliable and will not be focused on this study. The region, where the measurement artifact arises in EIS is

highlighted in red in the corresponding NFR spectrum in Figure 2(f). Furthermore, it is noted that the charge transfer coefficient for the de-/intercalation at the positive electrode, which is additionally parameterized via NFRA, is no longer 0.50 but 0.55.

By comparing the full-cell and half-cells EIS and NFR spectra, an assignment of the underlying processes is possible and interpreted according to our former work.<sup>[51]</sup> Firstly, one could notice the full-cell EIS comprises three semicircles, and the diffusion arc starts below 1 Hz (Figure 2(b)). The low-frequency semicircle (1–10<sup>2</sup> Hz) is predominantly impacted by the positive electrode (Figure 2(h)) and only slightly by the negative electrode (Figure 2(e)). By comparing with the NFR spectra, one can identify that the process within this frequency range is a charge transfer process, as nonlinear signals are visible in the designated frequency range.

Meanwhile, the mid-frequency (10<sup>2</sup>–10<sup>3</sup> Hz) and high-frequency semicircles (above 10<sup>3</sup> Hz) in the full-cell EIS originate from further processes at the negative electrode. Similar findings have also been reported in our previous work.<sup>[51,52]</sup> As these processes do not show nonlinearities in the NFR spectrum, linear processes can be assigned to these semicircles: 10<sup>2</sup>–10<sup>3</sup> Hz is the process at the SEI/electrolyte interface and across the SEI

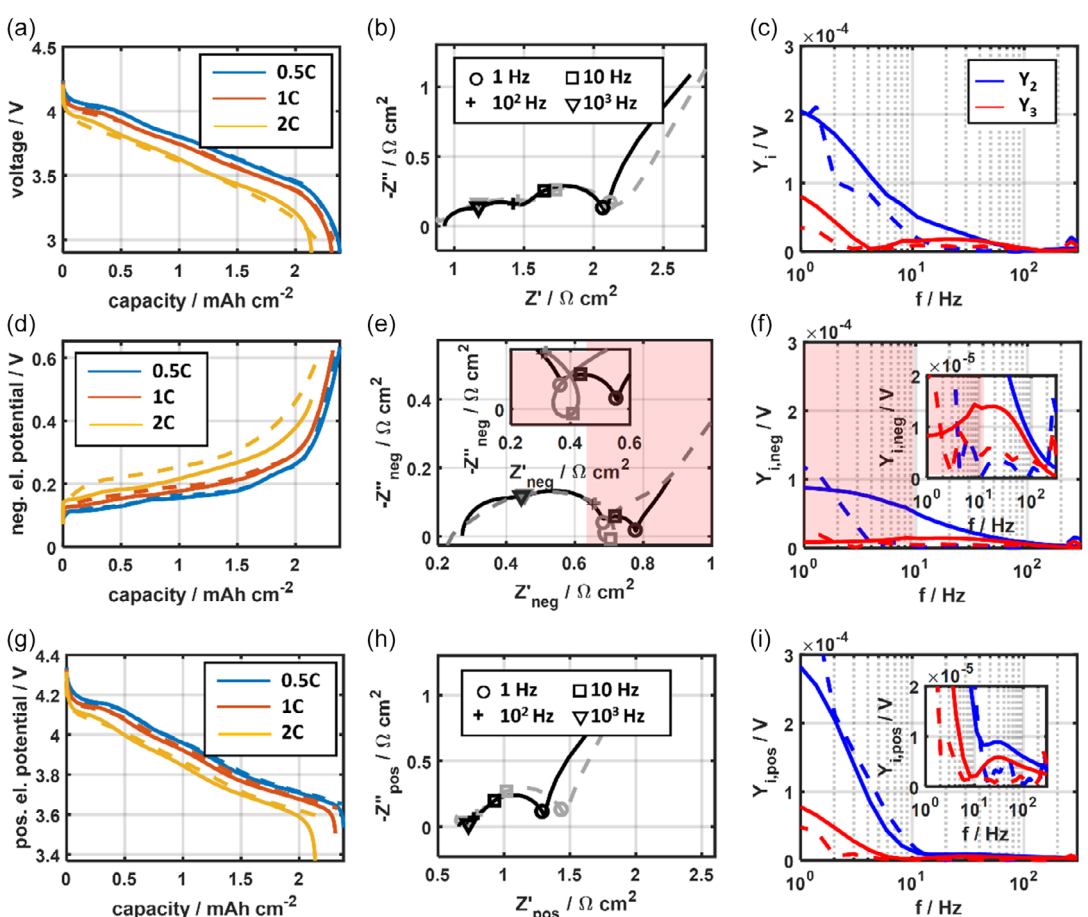


**Figure 2.** Simulation results reproducing experimental characterization after multistep parameterization strategy: discharge curves at 0.5, 1 C, and 2 C, EIS and NFRA at SoC 90% in full cell a–c), negative electrode d–f) and positive electrode g–i). Solid lines indicate the simulated and dashed lines the experimental results. The red-highlighted regions indicate the region that corresponds to the frequency range of EIS, in which the measurement artifact, that is, inductive loops appear (see inset of (e)).

**Table 2.** List of parameters obtained from the multistep parameterization strategy. Parameters with \* are uncertain as they show sensitivity neither toward discharge curves at different C-rates, EIS, nor NFRA as shown in supporting information S5.

Parameter	Unit	Negative	Separator	Positive
Maximum active material concentration, $c_{s,\max}$	[mol m <sup>-3</sup> ]	33,345	–	29,822
Initial active material concentration, $c_{s,0}$	[mol m <sup>-3</sup> ]	32,629	–	1,524
Solid diffusion coefficient, $D_s$	[m <sup>2</sup> s <sup>-1</sup> ]	1.8·10 <sup>-14</sup>	–	3.0·10 <sup>-15</sup>
Tortuosity, $\tau$	–	14.25*	1.36*	4.44*
Electrical conductivity, $\sigma_s$	[S m <sup>-1</sup> ]	209.6*	–	0.076
Contact resistance, $R_{cc}$	[Ω m <sup>2</sup> ]	1.5·10 <sup>-4</sup>	–	6.9·10 <sup>-5</sup>
SEI thickness, $d_{SEI}$	[nm]	85.8	–	–
Rate constant, $k_0$	[s <sup>-1</sup> ] (negative) [m s <sup>-1</sup> ] (positive)	30 (neg/SEI) 3.0·10 <sup>6</sup> (SEI/e)	–	2.6·10 <sup>-9</sup>
Double-layer capacitance, $C^{DL}$	[F m <sup>-2</sup> ]	20 (neg/SEI) 0.41 (SEI/e)	–	2
Charge transfer coefficient, $\alpha$	–	0.50 (neg/SEI) 0.50 (SEI/e)	–	0.55

layer. Further, we attribute the process above 10<sup>3</sup> Hz to the contact resistance between active material particles as well as at current collectors. The assignment of this frequency range to the contact resistance can also be observed in other publications.<sup>[53,54]</sup>

As mentioned previously in the multistep parameterization, kinetic parameters have been refined via NFRA. In the next section, we are going to study how these kinetic parameters influence the different characterization methods, that is, C-rate, EIS, and NFRA.

### 3.2. Kinetic Parameter Study

To gain a deeper understanding of the relationship between kinetic parameters and different characterization methods, a parameter study focusing on the kinetic parameters for this applied cell is performed.

As shown in Figure 3(a)–(c), the rate constant of the charge transfer process at the positive electrode  $k_{0,\text{pos}}$  has a significant impact on EIS and NFRA; this is especially notable in the frequency range attributed to the charge transfer process at

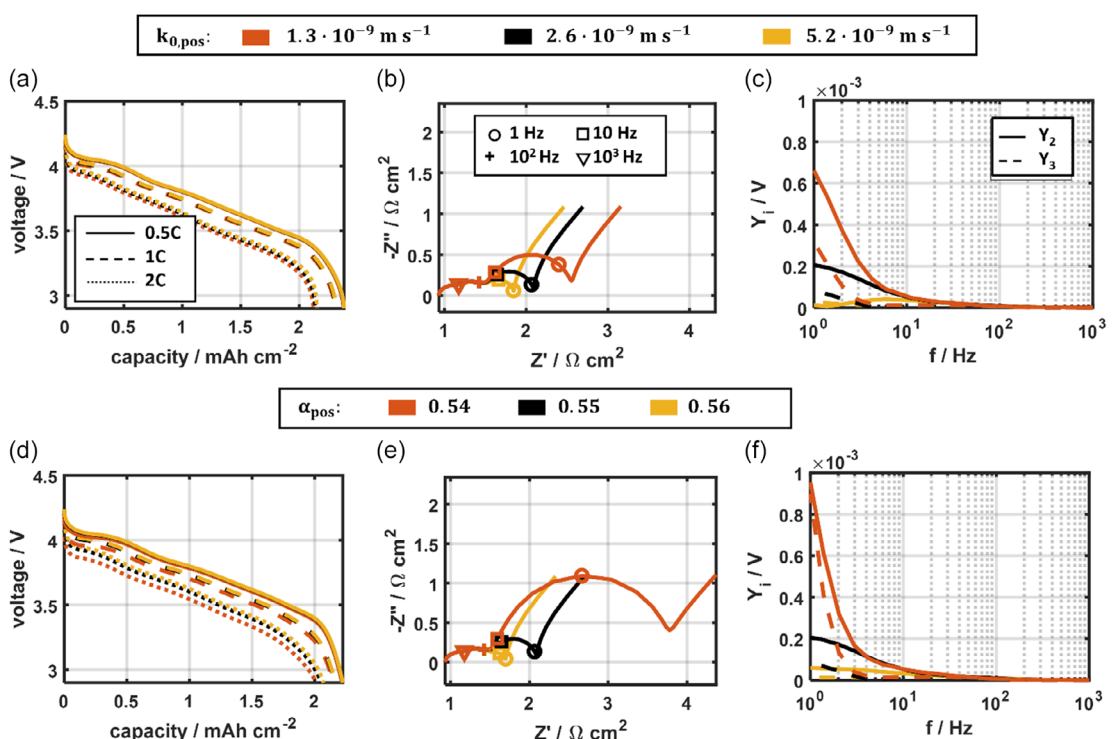


**Figure 3.** a–c) The impact of the rate constant of the de-/intercalation process at the positive electrode  $k_{0,\text{pos}}$  and the charge transfer coefficient at the positive electrode  $\alpha_{\text{pos}}$  on full cell d) C-rates, e) EIS, and f) NFRA at SoC 90%.

the positive electrode (1–10 Hz) for EIS and NFRA. In contrast, it has a negligible impact on the C-rate performance and impacts mainly at higher C-rate. By lowering  $k_{0,\text{pos}}$ , the impedance and NFR signals increase due to the decrease in the exchange current density, thus, leading to an increase in the overpotential for the respective process.

Besides the rate constant, it is also interesting to study the impact of the charge transfer coefficient at the positive electrode,  $\alpha_{\text{pos}}$  as the parameterization has resulted in a value of 0.55, not 0.50. As shown in Figure 3(d)–(f), a slight change in  $\alpha_{\text{pos}}$  shows a stronger impact than  $k_{0,\text{pos}}$  as  $\alpha_{\text{pos}}$  appears as an exponent in the exchange current density exponent as compared to the linearly related  $k_{0,\text{pos}}$ . In general, impedance and NFR signals, predominantly between 1 Hz and 10 Hz, increase significantly. Also, the discharge behavior at different C-rates is impacted. It shows a stronger drop in the initial voltage and hence a vertical shift of the voltage profile when  $\alpha_{\text{pos}}$  decreases.

Here, the variation in  $\alpha_{\text{pos}}$  impacts all frequency responses in EIS and NFRA, unlike previous findings by Wolff et al.<sup>[35]</sup> and Murbach et al.<sup>[34,55]</sup> which showed that  $\alpha_{\text{pos}}$  has distinct sensitivity toward second harmonics only. This is because the expression for the exchange current density used in this work is different from the above-mentioned publications. The exchange current density implemented by Wolff et al. and Murbach et al. is a constant. Meanwhile, in this work, the exchange current density is dependent on species concentrations and  $\alpha_{\text{pos}}$  (see Equation 11 in Supporting Information), considering the kinetics of the involved species at the interfaces as proposed by Doyle & Newman<sup>[56]</sup> and Smith & Wang's prior work.<sup>[57,58]</sup> In Supporting Information

Figure S3, it is further shown that when the exchange current density implemented in this work is assumed to be constant, a change in  $\alpha_{\text{pos}}$  leads to only a change in  $Y_2$ , while EIS and  $Y_3$  in NFRA remain unchanged, which is then similar to the findings of Wolff et al. and Murbach et al. Therefore, with the current implemented exchange current density formulation, the impact of  $\alpha_{\text{pos}}$  on EIS and  $Y_2$  and  $Y_3$  in NFRA cannot be clearly separated.

In addition, contrary to the work by Wolff et al. the variation in  $k_{0,\text{pos}}$  this work is also shown to be impacting not only EIS and  $Y_3$  but also  $Y_2$  in NFRA. This is because the parameter study here is performed based on the asymmetrical case, that is,  $\alpha_{\text{pos}}$  is equal to 0.55. If  $\alpha_{\text{pos}}$  is set to 0.50,  $k_{0,\text{pos}}$  only impacts EIS and  $Y_3$  in NFRA while  $Y_2$  remains the same, which is similar to Wolff et al.<sup>[35]</sup> (see Figure S4, Supporting Information). The Tafel plot analysis in the Supporting Information Figure S17 further illustrates that for  $\alpha_{\text{pos}} = 0.55$ , a decrease in  $k_{0,\text{pos}}$  leads to more asymmetric relation of current and potential.

The rate constant of the de-/intercalation process at the negative electrode  $k_{0,\text{neg/SEI}}$  is not as sensitive as that for the positive electrode for the investigated cell here. In Figure 4(a)–(c), one can notice that with the same relative variation in  $k_{0,\text{neg/SEI}}$  as  $k_{0,\text{pos}}$ , there is no visible change in the C-rate simulation, while there is only a slight increase in the EIS and NFR signals in the frequency range attributed to the charge transfer process at the negative electrode (1–10<sup>2</sup> Hz) when decreasing the rate constant. It is also shown here that  $k_{0,\text{neg/SEI}}$  simultaneously impacts  $Y_2$  besides EIS and  $Y_3$ , although  $\alpha_{\text{neg/SEI}}$  equals 0.50 in this parameter study. This is because the rate expression used for the charge transfer process here, unlike Butler–Volmer equation, is not symmetrical

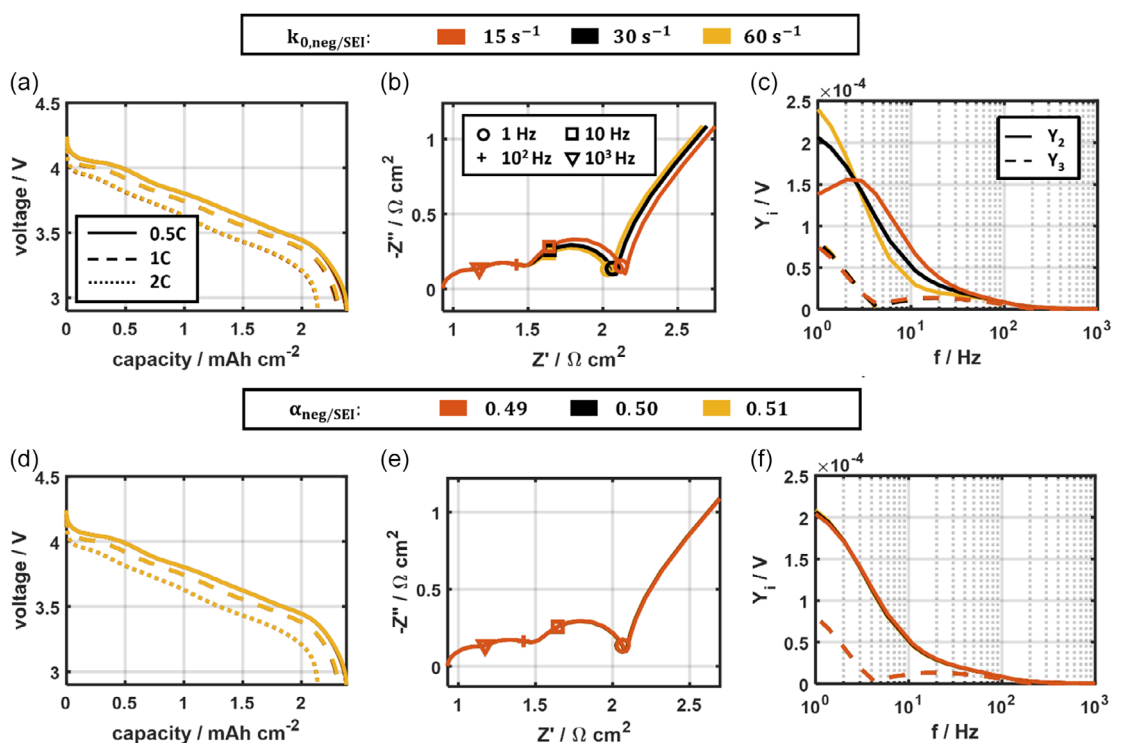


**Figure 4.** a–c) The impact of the rate constant of the de-/intercalation process at the negative electrode  $k_{0,\text{neg/SEI}}$  and the charge transfer coefficient at the negative electrode  $\alpha_{\text{neg/SEI}}$  on full cell d) C-rates, e) EIS, and f) NFRA at SoC 90%.

in nature. The asymmetrical behavior of the rate expression is shown in the Tafel plots in Figure S18, Supporting Information.

Further, as shown in Figure 4(d)–(f), the charge transfer coefficient  $\alpha_{\text{neg/SEI}}$  is not as sensitive as compared to  $\alpha_{\text{pos}}$ . It is shown that a similar quantitative change in  $\alpha_{\text{neg/SEI}}$  as  $\alpha_{\text{pos}}$  does not result in any change in C-rates, EIS and NFR spectra.

Meanwhile, a change in the rate constant of the ad-/desorption process between the electrolyte and SEI layer  $k_{0,\text{SEI/e}}$  has stronger sensitivity than  $k_{0,\text{neg/SEI}}$ . Especially, it shows a higher sensitivity in EIS and NFRA than in C-rate performance, as can be seen in Figure 5(a)–(c). A decrease in  $k_{0,\text{SEI/e}}$  results in an increase in the high-frequency ( $10^2$ – $10^3$  Hz) semicircle in EIS, indicating that the process at the SEI/electrolyte interface is impacted. It is also shown that the impedance of the de-/intercalation at the negative electrode ( $1$ – $10^2$  Hz) is mainly shifted horizontally toward a higher impedance but not increased in semicircle. This indicates that a change in ad-/desorption process at SEI/electrolyte shifts the quasi-steady state but does not change the dynamic of the de-/intercalation at the negative electrode.

A variation in the charge transfer coefficient in the corresponding process  $\alpha_{\text{SEI/e}}$  with the similar extent as  $\alpha_{\text{pos}}$  and  $\alpha_{\text{neg/SEI}}$  also shows a slight impact mainly on NFRA ( $Y_2$ ) as shown in Figure 5(f), which indicates mainly the charge transfer symmetry is affected. This outcome agrees with the finding of Wolff et al.<sup>[35]</sup> and Murbach et al.<sup>[34,55]</sup> that a change in charge transfer coefficient impacts only the second harmonics.

From the parameterization above, we could notice that for the analyzed cell the kinetic parameters at the negative electrode are not as sensitive as at positive electrode. Besides the kinetic

parameters, other transport-related parameters at the negative electrode such as tortuosity  $\tau$ , diffusion coefficient  $D_s$ , and electrical conductivity  $\sigma_s$  show the same behavior (see Supporting Information S5). Furthermore, it could be seen that the C-rate has a comparably lower sensitivity to the kinetic parameters. Therefore, EIS and NFRA are essential tools to identify these kinetic parameters. In general, the kinetic parameters, that is, the rate constant and the charge transfer coefficient, manifest complicated interactions in EIS and NFRA. Thus, in the subsequent section, a uniqueness study is carried out to distinguish the impact of the charge transfer coefficient and, at the same time, to demonstrate how to best identify these kinetic parameters.

### 3.3. Uniqueness Study

To understand how unique is the parameter set obtained from the multistep parameterization strategy and how to best identify the kinetic parameters, a uniqueness study is conducted. In our previous work,<sup>[32]</sup> such a study was performed on the C-rate test to resolve the identifiability of selected transport parameters such as solid diffusion coefficient and electronic conduction; in this study, we focus the uniqueness study on EIS to investigate the identifiability of the kinetic parameters, that is, the rate constants and charge transfer coefficients.

Here, we take the identified parameter set as the reference case. The rate constant and charge transfer coefficient are varied while all other parameters are kept constant. The outcome of the EIS simulation is then compared using the defined residual in

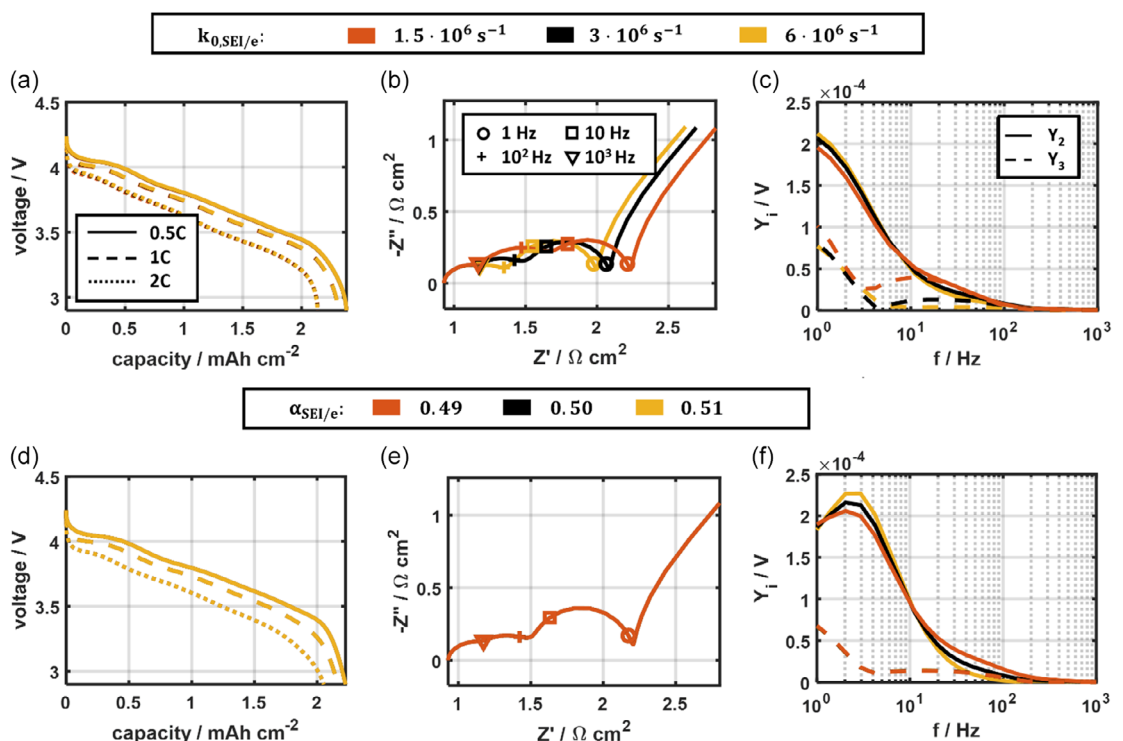


**Figure 5.** a–c) The impact of the rate constant of the ad-/desorption process at the SEI layer  $k_{0,\text{SEI/e}}$  and the charge transfer coefficient at the SEI layer  $\alpha_{\text{SEI/e}}$  on full cell d) C-rates, e) EIS, and f) NFRA at SoC 90%.

method section. Additionally, for EIS simulations with similar low residuals, the corresponding NFR spectra are further analyzed.

Firstly, **Figure 6** shows the outcome of the uniqueness study on EIS based on the kinetic parameters at the positive electrode, that is, rate constant  $k_{0,\text{pos}}$  and charge transfer coefficient  $\alpha_{\text{pos}}$ . From Figure 6(a), one could notice a dark blue diagonal line, which gives similarly minimal residuals. This means that multiple pairs of  $k_{0,\text{pos}}$  and  $\alpha_{\text{pos}}$  with the identified parameter set could deliver simulated full-cell EIS that best match with experimental ones.  $k_{0,\text{pos}}$  and  $\alpha_{\text{pos}}$  are thus not identifiable with EIS only. To further illustrate this, C-rate tests, EIS, and NFR spectra are simulated based on several pairs of  $k_{0,\text{pos}}$  and  $\alpha_{\text{pos}}$  that lie along the dark blue diagonal line as shown in Figure 6(a). As expected, the EIS spectra

with the selected  $k_{0,\text{pos}}$  and  $\alpha_{\text{pos}}$  pairs show no difference and give a good match to the experimental data (Figure 6(c)). There are also only marginal differences in the C-rate performance (Figure 6(b)). In NFR spectra, as shown in Figure 6(d) inset,  $Y_3$  is the same as EIS. Meanwhile,  $Y_2$  shows changes with a minimum when  $\alpha_{\text{pos}}$  approaches 0.50. Interestingly, one could see that  $\alpha_{\text{pos}} = 0.55$  could give a qualitative good agreement to the experimental  $Y_2$ . This further shows that NFRA could further refine a more unique parameter set that is obtained with EIS.

Next, **Figure 7** shows the result of the uniqueness study on EIS based on the kinetic parameters at the negative electrode: rate constant  $k_{0,\text{neg/SEI}}$  and charge transfer coefficient  $\alpha_{\text{neg/SEI}}$ . Similar to the positive electrode, the result also shows a dark blue line that

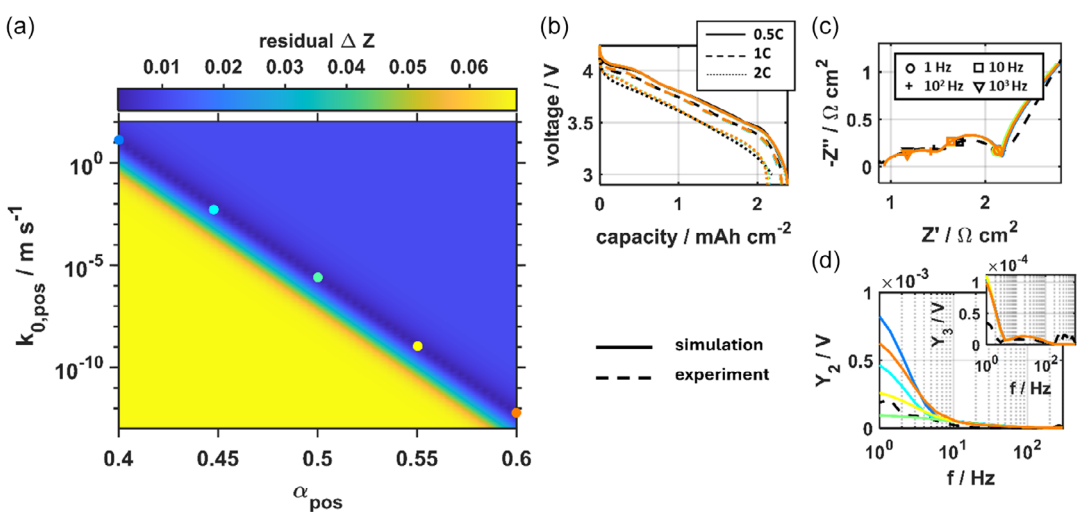


**Figure 6.** Uniqueness analysis based on the variation of the kinetic parameters at positive electrode, that is, rate constant  $k_{0,\text{pos}}$  and charge transfer coefficient  $\alpha_{\text{pos}}$ : a) residuals from the difference between simulated and experimental full cell EIS, respective simulated and experimental, b) discharge curves at several C-rates, c) EIS, and d) NFR spectra at SoC 90% based on the selected  $k_{0,\text{pos}}$  and  $\alpha_{\text{pos}}$  pairs along the dark blue diagonal line.

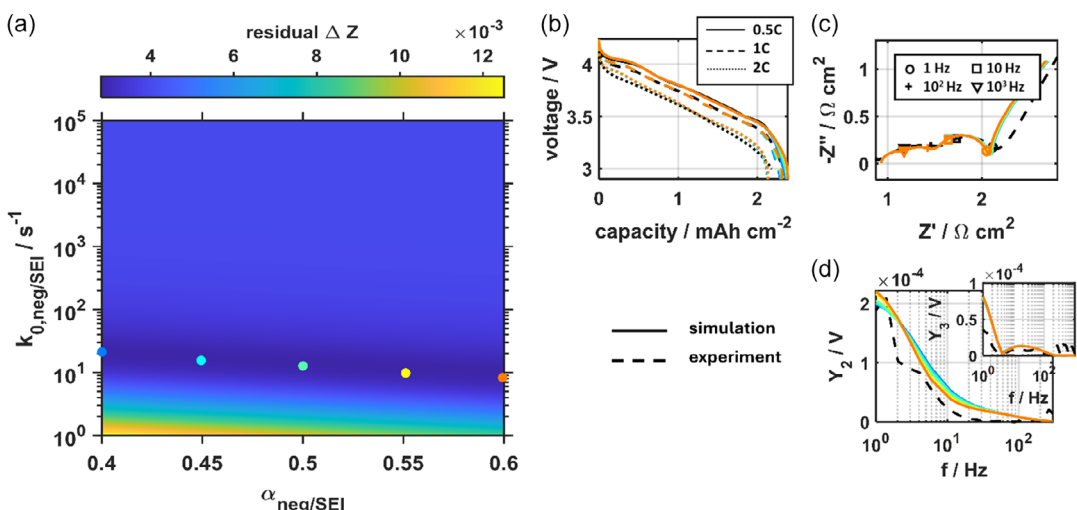


**Figure 7.** Uniqueness analysis based on the variation of the kinetic parameters at negative electrode, that is, rate constant  $k_{0,\text{neg/SEI}}$  and charge transfer coefficient  $\alpha_{\text{neg/SEI}}$ : a) residuals from the difference between simulated and experimental full cell EIS, respective simulated and experimental, b) discharge curves at several C-rates, c) EIS, and d) NFR spectra at SoC 90% based on the selected  $k_{0,\text{neg/SEI}}$  and  $\alpha_{\text{neg/SEI}}$  pairs along the dark blue diagonal line.

gives minimal residual from the comparison between simulated and experimental full-cell EIS (Figure 7(a)). However, in this case,  $k_{0,\text{neg}/\text{SEI}}$  varies only slightly between  $13\text{s}^{-1}$  and  $20\text{s}^{-1}$ . On the contrary, multiple optimal  $\alpha_{\text{neg}/\text{SEI}}$  exist that give simulated EIS that match to experiments. Hence,  $k_{0,\text{neg}/\text{SEI}}$  can be better determined as compared to  $\alpha_{\text{neg}/\text{SEI}}$ . Figure 7(b) to (d) show further the simulated C-rate performance, the simulated curves based on  $k_{0,\text{neg}/\text{SEI}}$  and  $\alpha_{\text{neg}/\text{SEI}}$  pairs that lie along the dark blue diagonal line. EIS and NFR spectra remain unchanged and give good match to the experimental result. This outcome matches well with the kinetic parameter study, as shown previously that for our cell  $\alpha_{\text{neg}/\text{SEI}}$  is insensitive to both EIS and NFRA characterization methods. Thus, it cannot be identified via these methods.

Meanwhile, the result of the uniqueness study of the kinetic parameters at the SEI/electrolyte interface, rate constant  $k_{0,\text{SEI}/e}$  and the charge transfer coefficient  $\alpha_{\text{SEI}/e}$ , is depicted in Figure 8. The result is similar to the uniqueness outcome of the kinetic parameters at the negative electrode: the optimal  $k_{0,\text{SEI}/e} = 3 \cdot 10^6 \text{s}^{-1}$  is identified via EIS parameterization, whereas  $\alpha_{\text{SEI}/e}$  could not be identified by EIS alone. Figure 8(b) to (d) show the simulated C-rate performance, EIS, and NFR spectra based on the selected  $k_{0,\text{SEI}/e}$  and  $\alpha_{\text{SEI}/e}$  pairs that lie along the dark blue line. It is shown that  $\alpha_{\text{SEI}/e}$  is possible to be determined via  $Y_2$ , as  $Y_2$  varies with the change in  $\alpha_{\text{SEI}/e}$  while C-rate tests, EIS, and  $Y_3$  remain almost constant. Here, it can be seen that  $\alpha_{\text{SEI}/e}$  is identified to be 0.50 that gives the best match to the experimental results.

In conclusion, the kinetic parameter pair at the positive electrode requires both EIS and NFRA methods for a unique identification. At the negative electrode/SEI interface as well as SEI/electrolyte interface, the rate constant can be identified by EIS. The charge transfer coefficient at the SEI/electrolyte interface can be further identified via NFRA whereas the charge transfer coefficient at the negative electrode is insensitive to either EIS or NFRA method, therefore it cannot be identified here. It should

be noted that here obtained sensitivities may be cell-specific, that is, a change in active material or cell balancing might lead to different limitations and sensitivities.

### 3.4. Comparison to Literature Values

In the following, we will compare the charge transfer coefficients that were obtained from our multistep parameterization strategy with the literature values.

For the positive electrode, the obtained charge transfer coefficient in this work (0.55) coincides with the reported ranges of charge transfer coefficients (0.48–0.58) regardless of the active materials. For instance, Hess et al. reported a charge transfer coefficient between 0.56 and 0.58 for lithium cobalt oxides (via GITT analysis)<sup>[38]</sup> and Heubner et al. obtained a charge transfer coefficient of 0.55 for lithium iron phosphates via Tafel plot analysis.<sup>[59]</sup> Ecker et al. determined a charge transfer coefficient of 0.517 for lithium nickel cobalt oxide using EIS superimposed with different bias currents and fit the charge transfer resistance with the Butler–Volmer equation.<sup>[28]</sup> However, to the authors' knowledge, only few works reported on the charge transfer coefficient for the active material–lithium nickel manganese cobalt oxides–811. Recently, Kirk et al. reported a small charge transfer coefficient of 0.48 via parameterization of Single Particle Model.<sup>[46]</sup> Nevertheless, the author only performed parameterization on full-cell measurements, as half-cell measurements are not assessable in commercial cell. Ji et al. identified a change in charge transfer coefficient from 0.50 to 0.61 for mixed lithium nickel manganese cobalt oxide with lithium manganese oxide when the cell aged.<sup>[48]</sup>

For negative electrode, there are discrepancies between the obtained charge transfer coefficient in this work (0.50) and the reported literature values (0.28–2.03). The reported charge transfer coefficients vary more significantly as compared to the one of positive electrode. Piao et al. used a charge transfer coefficient dependent exchange current density. By measuring and fitting

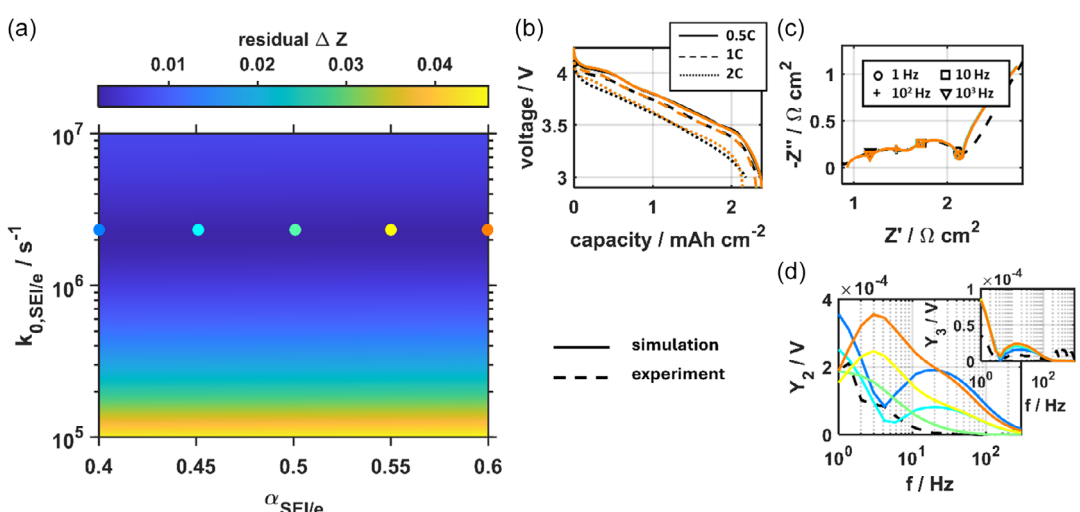


**Figure 8.** Uniqueness analysis based on the variation of the kinetic parameters at SEI interface, that is, rate constant  $k_{0,\text{SEI}/e}$  and charge transfer coefficient  $\alpha_{\text{SEI}/e}$ : a) residuals from the difference between simulated and experimental full cell EIS, respective simulated and experimental b) discharge curves at several C-rates, c) EIS and d) NFR spectra at SoC 90% based on the selected  $k_{0,\text{SEI}/e}$  and  $\alpha_{\text{SEI}/e}$  pairs along the dark blue diagonal line.

the exchange current densities at different lithium concentrations in graphite and in electrolyte, a charge transfer coefficient of 0.65 is determined.<sup>[60]</sup> Via the similar method, Chang et al. obtained the same charge transfer coefficient of 0.65 for graphite electrode.<sup>[61]</sup> Meanwhile, Dokko et al. used Tafel analysis method and found a range of charge transfer coefficients between 0.28 and 0.40 depending on the lithium concentration in the graphite electrode.<sup>[37]</sup> Ecker et al. found a charge transfer coefficient of 0.489 for the graphite electrode via EIS with DC bias.<sup>[28]</sup> Nevertheless, there are only few studies on the kinetic characterization of the silicon-graphite electrode. For example, Durdel et al. performed kinetic characterization on silicon-graphite electrode (Si – 69.7 wt%) and determined a charge transfer coefficient of 0.50.<sup>[62]</sup> Meanwhile, Chandrasekaran et al. identified a charge transfer coefficient of 2.03 for silicon electrode, which is much larger than the graphite electrode.<sup>[63]</sup> In general, for the graphite negative electrode, it is shown that there are widespread values for the charge transfer coefficient. This indicates that, as shown in our work, the charge transfer coefficient for the negative electrode cannot be easily determined.

On the contrary, the charge transfer coefficient for the SEI/electrolyte interface was barely investigated and mostly assumed to be symmetric:  $\alpha_{SEI/e} = 0.50$ ,<sup>[64–66]</sup> which matches with the one obtained in this work. To the authors' knowledge, only one work by Kindermann et al. took asymmetrical charge transfer coefficient (0.95) in the established SEI growth model.<sup>[67]</sup> Nonetheless, the model used in this work differs from the model by Kindermann et al. as we focus on state estimation of the battery rather than a SEI growth model of the battery. Also, Kindermann et al. did not parameterize the charge transfer coefficient but rather assumed a high irreversibility of the degradation process by taking a large charge transfer coefficient. Therefore, discrepancy in the charge transfer coefficient arises, and the charge transfer coefficient for the ad-/desorption process at the SEI/electrolyte interface is for the first-time in this work determined.

## 4. Conclusion

In the present study, we have introduced the multistep parameterization strategy for enhanced estimation of the kinetic parameters in the battery model. It is shown in the uniqueness study that the kinetic parameter set obtained via EIS only is not unique, that is, several pairs of rate constant and charge transfer coefficient can reproduce the experimental EIS. However, it can be improved by extending the parameterization procedure to include EIS and NFRA. With EIS + NFRA parameterization, the charge transfer coefficient can be further fine-tuned via  $Y_2$ .

The kinetics at the negative electrode show comparably low sensitivity compared to the positive electrode. As a result, the low sensitivity increases the uncertainty of the obtained parameter set at the negative electrode. To enhance the sensitivity and to provide a more comprehensive understanding of the nonlinear behavior across different operating regimes, EIS and NFRA characterizations can be performed at different

SOCs, as we have shown in our previous study that the EIS and NFR spectra appear to be different at different SOC.<sup>[14]</sup> Also, a possible future investigation could include the sensitivity analysis of the phase of the harmonics as well. Additionally, it is interesting to perform the parameterization in both charge and discharge directions to see whether the parameterization outcome involving NFRA could help in investigating the arising voltage hysteresis.

Furthermore, measurement artifacts like inductive loops, as shown in the half-cell data of the negative electrode exist, which might affect the accuracy of the parameterization outcome, not only impacting negative electrode but also positive electrode as well. Half-cell measurements from symmetrical cells can be conducted with NFRA also, which could eliminate the measurement artifact. Yet, the second harmonic in this case will be canceled out.<sup>[51]</sup> Therefore, parameterization via symmetrical cell configuration will not benefit from NFRA. As an outlook, for a unique parameterization of Li-ion battery which incorporates NFRA, another approach of half-cell measurements has to be developed, which has to be free from measurement artifact, for example, three-electrode setup with meshed reference electrode.<sup>[68]</sup> Lastly, we acknowledge the importance of validation study at different conditions to test the robustness of the outcome of this parameter estimation methodology, and we will consider it in the future.

## Acknowledgements

This project (17IND10 - LiBforSecUse) has received funding from the EMPIR program co-financed by the participating states and from the European Union's Horizon 2020 research and innovation program.

Open Access funding enabled and organized by Projekt DEAL.

## Conflict of Interest

The authors declare no conflict of interest.

## Author Contributions

**Hoon Seng Chan:** conceptualization (lead); formal analysis (lead); investigation (lead); methodology (lead); visualization (lead); writing—original draft (lead); writing—review and editing (lead); **Yan Ying Lee:** conceptualization (supporting); data curation (lead); formal analysis (supporting); investigation (supporting); methodology (supporting); **Daniel Witt:** methodology (supporting); software (lead); writing—review and editing (supporting); **Julian Ulrich:** methodology (supporting); writing—review and editing (supporting); **André Weber:** supervision (supporting); writing—review and editing (supporting); **Ulrike Krewer:** formal analysis (supporting); funding acquisition (lead); project administration (lead); supervision (lead); writing—review and editing (supporting).

## Data Availability Statement

The data presented in the manuscript are openly available in the KitOpen repository at DOI: 10.35097/s16mgsp2px2sp0h7.

**Keywords:** charge transfer coefficients • electrochemical impedance spectroscopy • harmonic response analysis • Newman models • parameterisation • uniqueness analysis

- [1] M. S. Hosen, J. Jaguemont, J. Van Mierlo, M. Berecibar, *iScience* **2021**, *24*, 102060.
- [2] V. Lucaferri, M. Quercio, A. Laudani, F. Riganti Fulginei, *Energies* **2023**, *16*, 7807.
- [3] D. Obuli Pranav, P. S. Babu, V. Indragandhi, B. Ashok, S. Vedhanayaki, C. Kavitha, *Sci. Rep.* **2024**, *14*, 16036.
- [4] W. Li, H. Zhang, B. van Vlijmen, P. Dechent, D. U. Sauer, *Energy Storage Mater.* **2022**, *53*, 453.
- [5] S. Carelli, W. G. Bessler, *J. Electrochem. Soc.* **2020**, *167*, 100515.
- [6] X. Feng, X. He, M. Ouyang, L. Wang, L. Lu, D. Ren, S. Santhanagopalan, *J. Electrochem. Soc.* **2018**, *165*, A3748.
- [7] F. Röder, S. Sonntag, D. Schröder, U. Kremer, *Energy Technol.* **2016**, *4*, 1588.
- [8] F. Wang, M. Tang, *Cell Rep. Phys. Sci.* **2020**, *1*, 100192.
- [9] U. Kremer, F. Röder, E. Harinath, R. D. Braatz, B. Bedürftig, R. Findeisen, *J. Electrochem. Soc.* **2018**, *165*, A3656.
- [10] M. Doyle, T. F. Fuller, J. Newman, *J. Electrochem. Soc.* **1993**, *140*, 1526.
- [11] M. Dubarry, D. Beck, *Acc. Mater. Res.* **2022**, *3*, 843.
- [12] A. Farmann, D. U. Sauer, *Appl. Energy* **2018**, *225*, 1102.
- [13] C. Fleischer, W. Waag, H.-M. Heyn, D. U. Sauer, *J. Power Sources* **2014**, *260*, 276.
- [14] H. S. Chan, E. J. F. Dickinson, T. P. Heins, J. Park, M. Gaberšček, Y. Y. Lee, M. Heinrich, V. Ruiz, E. Napolitano, P. Kauranen, E. Fedorovskaya, J. Moškon, T. Kallio, S. Mousavihashemi, U. Kremer, G. Hinds, S. Seitz, *J. Power Sources* **2022**, *542*, 231814.
- [15] K. A. Severson, P. M. Attia, N. Jin, N. Perkins, B. Jiang, Z. Yang, M. H. Chen, M. Aykol, P. K. Herring, D. Fragedakis, M. Z. Bazant, S. J. Harris, W. C. Chueh, R. D. Braatz, *Nat. Energy* **2019**, *4*, 383.
- [16] J. Newman, W. Tiedemann, *AIChE J.* **1975**, *21*, 25.
- [17] N. Legrand, S. Raël, B. Knosp, M. Hinaje, P. Desprez, F. Lapicque, *J. Power Sources* **2014**, *251*, 370.
- [18] D. Witt, F. Röder, U. Kremer, *Batter. Supercaps* **2022**, *5*, e202200067.
- [19] J. Christensen, J. Newman, *J. Electrochem. Soc.* **2004**, *151*, A1977.
- [20] A. M. Colclasure, K. A. Smith, R. J. Kee, *Electrochim. Acta* **2011**, *58*, 33.
- [21] C. von Lüders, J. Keil, M. Webersberger, A. Jossen, *J. Power Sources* **2019**, *414*, 41.
- [22] S. Hein, T. Danner, A. Latz, *ACS Appl. Energy Mater.* **2020**, *3*, 8519.
- [23] D. Witt, L. Bläubaum, F. Baakes, U. Kremer, *Batter. Supercaps* **2024**, *7*, e202400023.
- [24] M. A. Cabañero, N. Boaretto, M. Röder, J. Müller, J. Kallo, A. Latz, *J. Electrochem. Soc.* **2018**, *165*, A847.
- [25] K. Chayambuka, G. Mulder, D. L. Danilov, P. H. L. Notten, *J. Power Sources Adv.* **2021**, *9*, 100056.
- [26] I. O. Santos-Mendoza, J. Vázquez-Arenas, I. González, G. Ramos-Sánchez, C. O. Castillo-Araiza, *Int. J. Chem. React. Eng.* **2019**, *17*.
- [27] A. M. Colclasure, R. J. Kee, *Electrochim. Acta* **2010**, *55*, 8960.
- [28] M. Ecker, T. K. D. Tran, P. Dechent, S. Käbitz, A. Warnecke, D. U. Sauer, *J. Electrochem. Soc.* **2015**, *162*, A1836.
- [29] J. Landesfeind, H. A. Gasteiger, *J. Electrochem. Soc.* **2019**, *166*, A3079.
- [30] H. Lee, S. Yang, S. Kim, J. Song, J. Park, C.-H. Doh, Y.-C. Ha, T.-S. Kwon, Y. M. Lee, *Curr. Opin. Electrochem.* **2022**, *34*, 100986.
- [31] J. Schmalstieg, C. Rahe, M. Ecker, D. U. Sauer, *J. Electrochem. Soc.* **2018**, *165*, A3799.
- [32] V. Laue, F. Röder, U. Kremer, *J. Appl. Electrochem.* **2021**, *51*, 1253.
- [33] A. M. Bizeray, J. Kim, S. R. Duncan, D. A. Howey, *IEEE Trans. Control Syst. Technol.* **2019**, *27*, 1862.
- [34] M. D. Murbach, D. T. Schwartz, *J. Electrochem. Soc.* **2017**, *164*, E3311.
- [35] N. Wolff, N. Harting, F. Röder, M. Heinrich, U. Kremer, *Eur. Phys. J. Spec. Top.* **2019**, *227*, 2617.
- [36] T. Pajkossy, M. U. Ceblin, G. Mészáros, *J. Electroanal. Chem.* **2021**, *899*, 115655.
- [37] K. Dokko, N. Nakata, Y. Suzuki, K. Kanamura, *J. Phys. Chem. C* **2010**, *114*, 8646.
- [38] A. Hess, Q. Roode-Gutzmer, C. Heubner, M. Schneider, A. Michaelis, M. Bobeth, G. Cuniberti, *J. Power Sources* **2015**, *299*, 156.
- [39] Y. Li, Y. Qi, *Energy Environ. Sci.* **2019**, *12*, 1286.
- [40] H. P. Agarwal, *Electrochim. Acta* **1971**, *16*, 1395.
- [41] M. A. V. Devanathan, *Electrochim. Acta* **1972**, *17*, 1755.
- [42] K. Darowicki, J. Orlikowski, *Electrochim. Acta* **1998**, *44*, 433.
- [43] N. Xu, D. J. Riley, *Electrochim. Acta* **2013**, *94*, 206.
- [44] N. Harting, N. Wolff, U. Kremer, *Electrochim. Acta* **2018**, *281*, 378.
- [45] N. Harting, N. Wolff, F. Röder, U. Kremer, *Electrochim. Acta* **2017**, *248*, 133.
- [46] T. L. Kirk, A. Lewis-Douglas, D. Howey, C. P. Please, S. Jon Chapman, *J. Electrochem. Soc.* **2023**, *170*, 010514.
- [47] Y. Ji, D. T. Schwartz, *J. Electrochem. Soc.* **2023**, *170*, 123511.
- [48] Y. Ji, D. T. Schwartz, *J. Electrochem. Soc.* **2024**, *171*, 023504.
- [49] J. Ulrich, A. Lindner, T. Brake, M. Winter, S. Wiemers-Meyer, A. Weber, U. Kremer, *J. Power Sources* **2025**, 647C.
- [50] T. Vidaković-Koch, T. Miličić, L. A. Živković, H. S. Chan, U. Kremer, M. Petkovska, *Curr. Opin. Electrochem.* **2021**, *30*, 100851.
- [51] Y. Y. Lee, H. S. Chan, J. Ulrich, A. Weber, U. Kremer, *J. Electrochem. Soc.* **2024**, *171*, 070543.
- [52] H. Seng Chan, L. Bläubaum, D. Vijayshankar, F. Röder, C. Nowak, A. Weber, A. Kwade, U. Kremer, *Batter. Supercaps* **2023**, *6*, e202300203.
- [53] J. Illig, M. Ender, T. Chrobak, J. P. Schmidt, D. Klotz, E. Ivers-Tiffée, *J. Electrochem. Soc.* **2012**, *159*, A952.
- [54] J. P. Schmidt, T. Chrobak, M. Ender, J. Illig, D. Klotz, E. Ivers-Tiffée, *J. Power Sources* **2011**, *196*, 5342.
- [55] M. D. Murbach, V. W. Hu, D. T. Schwartz, *J. Electrochem. Soc.* **2018**, *165*, A2758.
- [56] M. Doyle, J. Newman, *Electrochim. Acta* **1995**, *40*, 2191.
- [57] K. Smith, C.-Y. Wang, *J. Power Sources* **2006**, *160*, 662.
- [58] K. A. Smith, C. D. Rahn, C.-Y. Wang, *Energy Convers. Manag.* **2007**, *48*, 2565.
- [59] C. Heubner, M. Schneider, A. Michaelis, *J. Power Sources* **2015**, *288*, 115.
- [60] T. Piao, S. M. Park, C. H. Doh, S. I. Moon, *J. Electrochem. Soc.* **1999**, *146*, 2794.
- [61] Y. C. Chang, J. H. Jong, G. T. K. Fey, *J. Electrochem. Soc.* **2000**, *147*, 2033.
- [62] A. Durdel, S. Friedrich, L. Hüskens, A. Jossen, *Batteries* **2023**, *9*, 558.
- [63] R. Chandrasekaran, T. F. Fuller, *J. Electrochem. Soc.* **2011**, *158*, A859.
- [64] S. Das, P. M. Attia, W. C. Chueh, M. Z. Bazant, *J. Electrochem. Soc.* **2019**, *166*, E107.
- [65] L. Liu, J. Park, X. Lin, A. M. Sastry, W. Lu, *J. Power Sources* **2014**, *268*, 482.
- [66] A. A. Tahmasbi, T. Kadyk, M. H. Eikerling, *J. Electrochem. Soc.* **2017**, *164*, A1307.
- [67] F. M. Kindermann, J. Keil, A. Frank, A. Jossen, *J. Electrochem. Soc.* **2017**, *164*, E287.
- [68] J. Costard, M. Ender, M. Weiss, E. Ivers-Tiffée, *J. Electrochem. Soc.* **2017**, *164*, A80.

Manuscript received: March 10, 2025

Revised manuscript received: April 25, 2025

Version of record online: